

See discussions, stats, and author profiles for this publication at: <https://www.researchgate.net/publication/263959478>

# Phase-Structure Effects of Electrospun TiO<sub>2</sub> Nanofiber Membranes on As(III) Adsorption

ARTICLE in JOURNAL OF CHEMICAL & ENGINEERING DATA · DECEMBER 2012

Impact Factor: 2.04 · DOI: 10.1021/jc301017q

CITATIONS

12

READS

58

4 AUTHORS, INCLUDING:



Xiang Li

Jilin University

55 PUBLICATIONS 460 CITATIONS

SEE PROFILE



Zhenyu Li

Jilin University

48 PUBLICATIONS 1,305 CITATIONS

SEE PROFILE



Ce Wang

Jilin University

209 PUBLICATIONS 4,335 CITATIONS

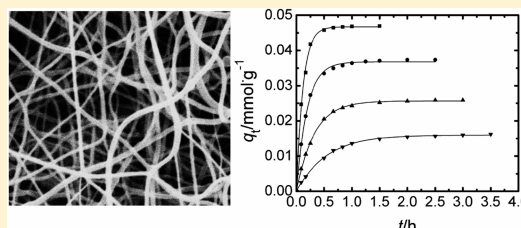
SEE PROFILE

# Phase-Structure Effects of Electrospun TiO<sub>2</sub> Nanofiber Membranes on As(III) Adsorption

Dinhthao Vu, Xiang Li,\* Zhenyu Li, and Ce Wang\*

Alan G. MacDiarmid Institute, Jilin University, Changchun 130012, P. R. China

**ABSTRACT:** TiO<sub>2</sub> nanofibers (NFs) with different phases such as amorphous, anatase, mixed anatase–rutile, and rutile have been prepared by combining the electrospinning technique with the subsequent process of heat treatment or acidic-dissolution method. The obtained NFs are characterized by a Fourier transform infrared spectrometer (FT-IR), X-ray photoelectron spectroscopy (XPS), X-ray diffraction (XRD), scanning electron microscopy (SEM), transmission electron microscopy (TEM), and N<sub>2</sub> adsorption–desorption isotherm measurements. Phase structure effects of electrospun TiO<sub>2</sub> NFs on As(III) adsorption behaviors have been investigated. The results showed a significant effect of the phase structures of TiO<sub>2</sub> NFs on As(III) adsorption rates and capacities. Amorphous TiO<sub>2</sub> NFs have the highest As(III) adsorption rate and capacity in the investigated samples, which can be attributed to its higher surface area and porous volume. This research provides a simple and low-cost method for phase-controlled fabrication of TiO<sub>2</sub> NFs and application for effective removal of arsenic from aqueous solution.



## 1. INTRODUCTION

Arsenic has been recognized for centuries as one of the most toxic pollutants in an aqueous environment.<sup>1</sup> Long-term exposure to arsenic-contaminated water causes serious health problems in the human bodies such as skin, lung, stomach, urinary bladder, liver, and kidney cancers.<sup>2</sup> Since arsenic has negative impacts on human health, the World Health Organization (WHO) and the United States Environmental Protection Agency (USEPA) have limited the concentration of arsenic to 10  $\mu\text{g}\cdot\text{L}^{-1}$  in drinking water.<sup>3</sup> In an aqueous environment, arsenic mostly existed in the inorganic form as oxyanions of trivalent (As(III)) and pentavalent arsenic (As(V)). As(III) is more toxic and difficult to remove from aqueous environment than As(V).<sup>4</sup> Thus, the effective removal of As(III) from water systems is very important to protect public health. Recently, researchers have demonstrated that nanocrystalline TiO<sub>2</sub> is effective for the removal of As(III) from aqueous solutions. Adsorption of As(III) by TiO<sub>2</sub> has been also investigated by many authors.<sup>1,5–12</sup> However, most of these reports have been focused on the removal of As(III) based on TiO<sub>2</sub> nanoparticles. Although TiO<sub>2</sub> nanoparticles have higher As(III) removal capacities than the bulk TiO<sub>2</sub> material,<sup>12</sup> they easily self-aggregate in aqueous solution, which results in a fast reduction of active surface area.<sup>13</sup> Moreover, it is difficult to separate TiO<sub>2</sub> nanoparticles from aqueous solution after adsorption. These disadvantages have limited their practical applications. Electrospun TiO<sub>2</sub> NFs are expected to solve these problems because they combine the advantages of nanoparticles and thin film.<sup>14,15</sup> Recently, our group has reported the preparation of TiO<sub>2</sub> nanofibers via an electrospinning method and their application for Cu(II) adsorption.<sup>16</sup> However, the effects of the phase structures of TiO<sub>2</sub> NFs on adsorption behaviors have not been investigated.

The physical and chemical surface properties of TiO<sub>2</sub> NFs are influenced by polymorphs and their structures. The surface area and porous volume are important parameters of TiO<sub>2</sub> NFs due to its direct impact on the adsorption behaviors. Thus, the controllable fabrication of the phase structures of TiO<sub>2</sub> NFs is very important for their applications.

In this study, a series of TiO<sub>2</sub> NFs with different phase structures was prepared by an electrospinning technique with subsequent acidic-dissolution or heat treatment process. The As(III) adsorption based on 1D electrospun TiO<sub>2</sub> NFs with different phases has been demonstrated.

## 2. EXPERIMENTAL SECTION

**2.1. Chemicals.** Chemicals used in this study are listed in Table 1. All reagents were of analytical grade and used without further purification. Deionized water was prepared by a Barnstead NANOpure water purification system. Stock solution (0.0133 mmol·kg<sup>-1</sup>) of As(III) was prepared by dissolving the appropriate amounts of NaAsO<sub>2</sub> into deionized water and

Table 1. Chemicals Chosen for This Present Study

chemical name	molecular formula	source	mass fraction purity
PVP <sup>a</sup>	(C <sub>6</sub> H <sub>9</sub> NO) <sub>n</sub>	Sigma, Aldrich	0.996
tetrabutyl titanate	Ti(OC <sub>4</sub> H <sub>9</sub> ) <sub>4</sub>	Sigma, Aldrich	0.999
acetic acid	CH <sub>3</sub> COOH	Beijing, China	0.999
ethanol	C <sub>2</sub> H <sub>5</sub> OH	Beijing, China	0.999
sodium arsenic	NaAsO <sub>2</sub>	Fluka, Aldrich	0.998

<sup>a</sup>Poly(vinyl pyrrolidone)/M<sub>n</sub> = 1 300 000.

Received: August 2, 2012

Accepted: December 3, 2012

Published: December 11, 2012

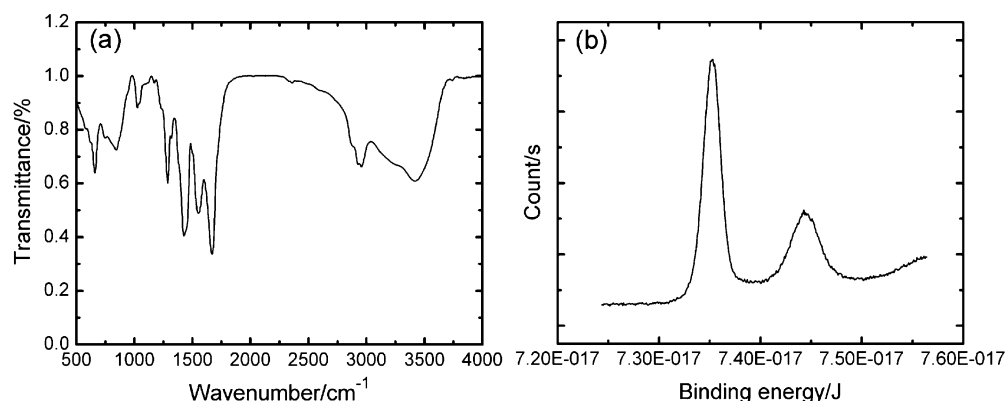


Figure 1. FT-IR spectrum of PVP/TiO<sub>2</sub> NFs (a) and XPS spectra of Ti 2p (b).

stored in a dark place to prevent oxidation. Working standard solutions were prepared by diluting the stock solution.

**2.2. Characterization.** The morphology of the NFs was observed by scanning electron microscopy (SEM, Shimadzu SSX-550). Transmission electron microscope (TEM) measurements were performed on a JEOL JEM 2000EX at 200 kV. A Fourier transform infrared (FT-IR) spectrum was recorded on a Bruker VECTOR-22 FT-IR spectrometer from 500 cm<sup>-1</sup> to 4000 cm<sup>-1</sup> using powder-pressed KBr pellets at room temperature. X-ray photoelectron spectroscopy (XPS, ESCALABMK II) was used to confirm the binding energy of elements. The phase structure of the samples was characterized by X-ray diffraction (XRD, Siemens D5005 diffractometer using Cu K $\alpha$  radiation) in the scan range  $2\theta$  between 10° and 80°. The Brunauer–Emmett–Teller (BET) surface areas and porous volumes of the samples were measured from N<sub>2</sub> adsorption–desorption isotherms (Micromeritics ASAP 2000 apparatus at 77 K). The concentrations of As(III) were determined using an inductive coupled plasma emission spectrometer (ICP) (PerkinElmer OPTIMA 3300DV, USA). The pH values of the adsorption solutions were measured using a pH meter (Orion 410A+, Thermo).

### 2.3. Synthesis of Amorphous and Crystalline TiO<sub>2</sub> NFs.

In the first step, we prepared precursor nanofibers (PVP/TiO<sub>2</sub> NFs) using an electrospinning technique.<sup>16,17</sup> In this procedure, 1.5 g of Ti(OBu)<sub>4</sub> was mixed with 3 mL of acetic acid and 3 mL of ethanol under vigorous stirring for 0.5 h. Subsequently, this solution was quickly added into 7.5 mL of ethanol containing 0.45 g of poly(vinyl pyrrolidone) (PVP). This mixing was followed by a vigorous stirring for 0.5 h for electrospinning. All of experiments were done in a dried environment to prevent the hydrolysis reaction of Ti(OBu)<sub>4</sub>. Then, the as-prepared gel was immediately loaded into a glass syringe with a needle of 1 mm in diameter at the tip and connected to high-voltage power supply (Gamma High Voltage Supply, Ormond Beach, FL, USA (ES 30-0.1P)). An electric potential of 15 kV was provided between the tip of the spinning nozzle and the collector at a distance of 20 cm. Finally, the amorphous TiO<sub>2</sub> NFs were prepared by immersing the as-received PVP/TiO<sub>2</sub> NFs into a vial containing aqueous CH<sub>3</sub>COOH (pH = 5) solution at room temperature for 12 h to remove the PVP matrix. The crystalline TiO<sub>2</sub> NFs with different phases such as anatase, mixed anatase–rutile, and rutile were fabricated by sintering the PVP/TiO<sub>2</sub> NFs at 723 K, 823 K, and 973 K for 3 h in air to remove the PVP and to transform the amorphous TiO<sub>2</sub> into crystalline TiO<sub>2</sub>.

**2.4. Adsorption Behaviors.** The TiO<sub>2</sub> NFs with different phases such as amorphous, anatase, mixed anatase–rutile, and rutile were used as adsorbents. The batch technique was used in adsorption experiments. The adsorption experiments were conducted in 250 mL flasks, each of which contained 100 mL of As(III) solution. The kinetics of As(III) adsorption on TiO<sub>2</sub> NFs were performed by adding 0.025 g of TiO<sub>2</sub> NFs into 100 mL of solution of As(III) (0.0133 mmol·kg<sup>-1</sup>). The solution was controlled at 298 ± 1.6 K under magnetic stirring at a rate of 250 ± 5 rpm. The solution pH in all of the tests was maintained at pH = 7.0 ± 0.1 by adding either 0.1 mol·kg<sup>-1</sup> HCl or 0.1 mol·kg<sup>-1</sup> NaOH solutions. At each predetermined time point in intervals of 0.1 to 4 h, a 5.0 mL solution was withdrawn from the suspension. Then, the samples were filtered through a 0.25 μm pore size membrane filter, and the As(III) concentration in the filtered solution was determined by an inductive coupled plasma emission spectrometer (ICP). The adsorption isotherms of As(III) on TiO<sub>2</sub> NFs were obtained by adding 0.025 g of TiO<sub>2</sub> samples into a series of flasks containing 100 mL As(III) solution of varying initial concentrations, ranging from 0.00133 mmol·kg<sup>-1</sup> to 0.0133 mmol·kg<sup>-1</sup>. The pH value was adjusted to 7.0 ± 0.1. The flasks were kept at 298 ± 1.6 K for 4 h. All of the experiments were conducted in the dark to prevent As(III) oxidation. After reached the adsorption equilibrium, the suspension was filtered to separate TiO<sub>2</sub> from the solution, and the As(III) concentrations in the filtered solution were analyzed by ICP. Triplicate adsorption experiments were conducted, and average results were reported.

The adsorption amount of As(III) onto each sample was calculated using the following equation:

$$q_e = \frac{(C_0 - C_e)V}{m} \quad (1)$$

where  $C_0$  and  $C_e$  are the initial and the equilibrium concentrations of the As(III) solution (mmol·kg<sup>-1</sup>),  $V$  is the volume of the As(III) solution (L),  $m$  is the weight of the adsorbent (g), and  $q_e$  is the equilibrium adsorption capacity (mmol·g<sup>-1</sup>).

## 3. RESULTS AND DISCUSSION

**3.1. Characterization of Materials.** A FT-IR spectrum is used to confirm the existence of PVP within the PVP/TiO<sub>2</sub> composite as shown in Figure 1a. The characteristic peaks at 1425 cm<sup>-1</sup> is assigned to the C–H vibration; the peak at 1545 cm<sup>-1</sup> corresponds to the ring C–C stretching; the absorption band at 2924 cm<sup>-1</sup> and 2854 cm<sup>-1</sup> can be assigned to the CH<sub>3</sub>

and CH<sub>2</sub> stretching vibrations; the peak at 1650 cm<sup>-1</sup> is attributed to the C=O stretching vibrations; the peak at 1285 cm<sup>-1</sup> is related to the tertiary amine C–N stretching vibrations, and the peaks in the region from 3180 cm<sup>-1</sup> to 3527 cm<sup>-1</sup> are stretching vibrations of the –OH group. All of these peaks are similar to the IR character of PVP reported before.<sup>18</sup> In addition, the peak at 650 cm<sup>-1</sup> can be assigned to the Ti–O bond.<sup>19</sup> The Ti 2p XPS spectra, which are more precise to confirm the existence of TiO<sub>2</sub> in the composite, are shown in Figure 1b. The peaks at 7.35·10<sup>-17</sup> J (Ti 2p<sub>3/2</sub>) and 7.44·10<sup>-17</sup> J (Ti 2p<sub>1/2</sub>) are assigned to Ti<sup>4+</sup> (TiO<sub>2</sub>).<sup>20</sup> On the basis of FT-IR and XPS results, we determine that the TiO<sub>2</sub> has successfully composited with PVP.

Figure 2 presents the XRD patterns of the samples. No peaks of crystalline phase are detected, which indicate that both the

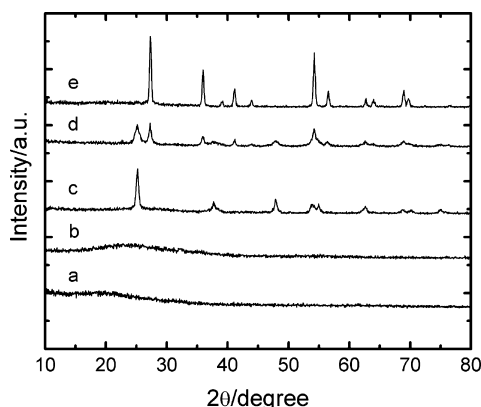


**Figure 2.** XRD patterns of the PVP/TiO<sub>2</sub> NFs (a), amorphous TiO<sub>2</sub> NFs (b), and crystalline TiO<sub>2</sub> NFs sintered at 723 K (c), 823 K (d), and 973 K (e).

PVP/TiO<sub>2</sub> NFs and TiO<sub>2</sub> NFs synthesized by the acidic-dissolution method are amorphous, while TiO<sub>2</sub> NFs prepared by the heat treatment method are crystalline phase. XRD tests shown that, with increasing sintering temperature, TiO<sub>2</sub> gradually transformed from anatase to rutile phase. The NFs sintered at 723 K are identified as anatase crystalline structure (JCPDS: 21-1272), and the NFs sintered at 823 K consist of the mixed anatase and rutile phases, while the NFs sintered at 973 K show the presence of pure rutile phase (JCPDS: 21-1276). The phase composition of crystalline TiO<sub>2</sub> NFs can be calculated from the integrated intensities at 2θ = 25.3° (101) for anatase and the peak at 2θ = 27.9° (110) for rutile. The weight fraction of the rutile phase in the TiO<sub>2</sub> NFs,  $W_R$ , is calculated using the following formula:<sup>21</sup>

$$W_R = \frac{A_R}{0.886A_A + A_R} \quad (2)$$

where  $A_A$  and  $A_R$  represent the integrated intensity of the anatase (101) and rutile (110) peaks, respectively.

**Table 2.** Physicochemical Properties of TiO<sub>2</sub> NFs<sup>a</sup>

TiO <sub>2</sub> NFs	$W_A/\%$	$W_R/\%$	$L/\text{nm}$	$S_{\text{BET}}/\text{m}^2\cdot\text{g}^{-1}$	$D_p/\text{nm}$	$V_p/\text{cm}^3\cdot\text{g}^{-1}$
amorphous				65	6.34	0.187
723 K	100	0	7.44	42	9.58	0.138
823 K	42.33	57.67	28.31	25	11.84	0.086
973 K	0	100	44.11	12	17.82	0.044

<sup>a</sup> $W_A$ : phase contents of anatase;  $W_R$ : phase contents of rutile;  $L$ : crystalline size;  $S_{\text{BET}}$ : BET surface area;  $D_p$ : pore size;  $V_p$ : total pore volume.

The crystalline size of the samples is calculated according to the Debye–Scherrer equation.

$$L = 0.89\lambda / (B \cos \theta) \quad (3)$$

where  $L$  is the crystalline size,  $\lambda$  is the X-ray wavelength,  $B$  is the peak width at half-maximum height, and  $\theta$  is the diffraction angle.

The calculation results are shown in Table 2. As seen in the table, the crystalline size increased significantly when sintering temperature ( $T_s$ ) increased from 723 K to 973 K, which can be attributed to the heat of the phase transformation from anatase to rutile promoted the growth of crystalline grains. These changes of phase composition and crystalline size as a function of  $T_s$  are commonly observed with synthetic TiO<sub>2</sub> in earlier reports.<sup>22,23</sup>

The morphologies of nanofibrous membranes are observed by SEM, and the results are shown in Figure 3. It can be seen

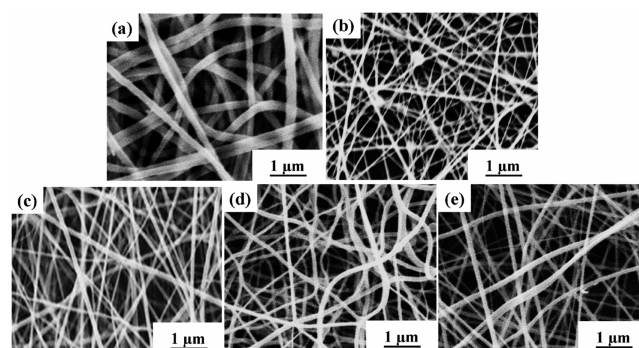


**Figure 3.** SEM images of electrospun PVP/TiO<sub>2</sub> NFs (a), amorphous TiO<sub>2</sub> NFs (b), and crystalline TiO<sub>2</sub> NFs (c, d, e).

that the membranes are composed of numerous, randomly oriented nanofibers, and the diameters of the PVP/TiO<sub>2</sub> NFs are in the range of 150 nm to 250 nm (Figure 3a). During the electrospinning process, as the solution was gradually ejected from the spinneret, Ti(OBu)<sub>4</sub> hydrolyzed by reacting with trace moisture in air to form particles of amorphous TiO<sub>2</sub> in a PVP matrix. The PVP acted as a template and shape-controlling agent. The PVP could also prevent the small particles of amorphous TiO<sub>2</sub> from aggregating into larger ones.<sup>24–26</sup> After being immersed in an aqueous CH<sub>3</sub>COOH (pH = 5) solution at the room temperature to dissolve the organic constituent of PVP, the average diameter of NFs decreased to 85 nm (Figure 3b). This size reduction could be attributed to the loss of PVP from the NFs. Because of a small diameter for the NFs, the amorphous TiO<sub>2</sub> NFs can be formed by the accumulation of very small and uniform amorphous TiO<sub>2</sub> nanoparticles. The SEM images of the crystalline TiO<sub>2</sub> NFs shown in Figure 3c–d indicated that the NFs still remained as continuously long nanofibrous shape, and their average diameters (100 nm) did not change significantly. The growth of grains in crystalline



TiO<sub>2</sub> NFs was not seen by SEM. Thus, the morphologies of the crystalline TiO<sub>2</sub> NFs are further observed by TEM. Figure 4a–c

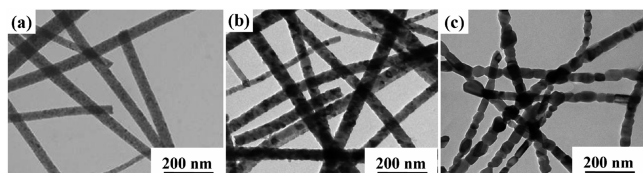


**Figure 4.** TEM images of crystalline TiO<sub>2</sub> NFs prepared by sintering the electrospun PVP/TiO<sub>2</sub> NFs in air at 723 K (a), 823 K (b), and 973 K (c).

shows TEM images of the crystalline TiO<sub>2</sub> NFs. It is obvious that crystalline TiO<sub>2</sub> NFs are composed of TiO<sub>2</sub> nanoparticles, aggregated along fiber orientation. It could be seen the morphology of grains in the TiO<sub>2</sub> NFs (823 K) with a grain size of ~20 nm to 30 nm. When the sintering temperature was increased to 973 K, the grains grew larger with a grain size of ~40 nm to 60 nm, which is in agreement with the XRD results.

The BET surface area ( $S_{\text{BET}}$ ) and pore volume ( $V_p$ ) parameters are shown in Table 2. The  $S_{\text{BET}}$  of the amorphous TiO<sub>2</sub> NFs is higher than that of the crystalline TiO<sub>2</sub> NFs. For crystalline TiO<sub>2</sub> NFs, the  $S_{\text{BET}}$  decreases dramatically from anatase TiO<sub>2</sub> to rutile TiO<sub>2</sub> phase. This can be explained by the fact that the  $S_{\text{BET}}$  of the TiO<sub>2</sub> NFs formed between aggregated TiO<sub>2</sub> nanoparticles should depend on the size of TiO<sub>2</sub> nanoparticles. As the grain size became larger with increasing sintering temperature, the  $S_{\text{BET}}$  would decrease. The  $V_p$  also decreased from amorphous TiO<sub>2</sub> to crystalline TiO<sub>2</sub> phase. Similar changes of  $S_{\text{BET}}$  and  $V_p$  caused by sintering have been reported.<sup>7</sup> This has been attributed to the collapse of the porous structure, the growth of grains, and phase transformation.<sup>27</sup>

Figure 5 presents the N<sub>2</sub> adsorption–desorption isotherm curves of TiO<sub>2</sub> samples. For the amorphous TiO<sub>2</sub> NFs, the

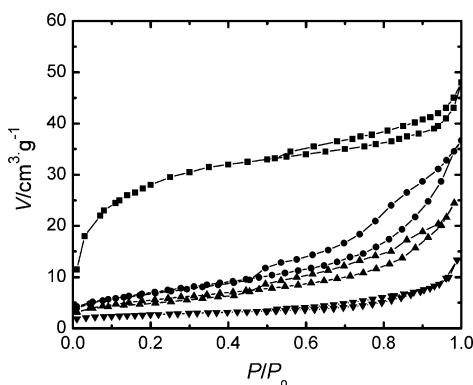


**Figure 5.** N<sub>2</sub> adsorption–desorption isotherms curves of TiO<sub>2</sub> samples. ■, amorphous; ●, anatase; ▲, anatase/rutile; ▼, rutile TiO<sub>2</sub> NFs;  $P/P_0$ : relative pressure;  $V$ : volume adsorbed.

isotherm curve is a combination of types I and IV isotherms (Brunauer–Deming–Deming–Teller (BDDT) classification) with two distinct areas; the isotherm curve exhibits high adsorption at low relative pressure, showing the presence of micropores (type I). However, the isotherm curve exhibits a small hysteresis loop at high relative pressure, indicating that the sample contained a small amount of mesopores (type IV).<sup>27,28</sup> The isotherms corresponding to the anatase TiO<sub>2</sub> NFs

and mixed anatase–rutile TiO<sub>2</sub> NFs are type IV isotherms according to BDDT classification with type H3 hysteresis loops, confirming the presence of mesopores on NFs surface.<sup>27–29</sup> These mesopores can be formed by the aggregation of TiO<sub>2</sub> nanoparticles along the fiber orientation during sintering process. For rutile TiO<sub>2</sub> NFs, the isotherm curve is the type II isotherm by BDDT classification.<sup>28,29</sup> The type II isotherm is characteristic for nonporous and macroporous adsorbents.<sup>28–30</sup>

**3.2. Adsorption Kinetics.** Adsorption kinetics is performed to evaluate both the equilibrium time and the rate of As(III) adsorption. The equilibrium time is one of the important parameters for subsequent adsorption isotherm studies. Figure 6 displays the effect of contact time on the removal of As(III).

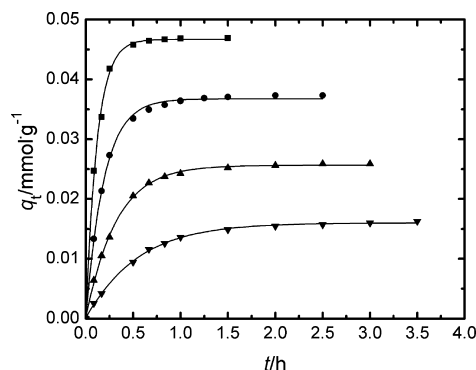


**Figure 6.** Kinetics of As(III) adsorption onto TiO<sub>2</sub> samples. ( $C_{0,\text{As(III)}}$ : 0.0133 mmol·kg<sup>−1</sup>; dosage of adsorbent: 0.25 kg·m<sup>−3</sup>; pH 7.0 ± 0.1; 298 K ± 1.6 K). ■, amorphous; ●, anatase; ▲, anatase/rutile; ▼, rutile TiO<sub>2</sub> NFs.

It demonstrated that the As(III) adsorption capacity increased with increasing contact time until an equilibrium was established between the solid phase and the liquid phase in the adsorption system. The removal of As(III) by amorphous TiO<sub>2</sub> NFs occurred rapidly and reached adsorption equilibrium within 1 h, while for crystalline TiO<sub>2</sub> NFs, this time is prolonged from 1.5 h to 3 h. To ensure the equilibrium adsorption of the As(III) on the TiO<sub>2</sub> NFs, a contact time of 4 h was chosen for subsequent adsorption isotherm studies.

To evaluate the rate of As(III) adsorption on TiO<sub>2</sub> NFs with different phases, the pseudosecond-order model was applied to analyze the experimental data. The pseudosecond-order model has been commonly used to describe chemical adsorption process of pollutants from aqueous solutions in recent years.<sup>31</sup>

The pseudosecond-order adsorption kinetic rate equation is in the following form:

$$\frac{t}{q_t} = \frac{1}{k_2 q_e^2} + \frac{1}{q_e} t \quad (4)$$

where  $q_e$  is the equilibrium adsorption capacity (mmol·g<sup>−1</sup>) and  $q_t$  is the adsorption capacity at the time  $t$  of As(III) on adsorbents (mmol·g<sup>−1</sup>).

$k_2$  is the pseudosecond-order rate constant (g·mmol<sup>−1</sup>·h<sup>−1</sup>), which is determined from a plot of  $t/q_t$  versus  $t$ .

The initial adsorption rate  $\nu$  (mmol·g<sup>−1</sup>·h<sup>−1</sup>) can be used to evaluate the adsorption rate.<sup>32</sup>

$$\nu = k_2 q_e^2 \quad (5)$$

The kinetic parameters obtained in fitting the experimental data are represented in Table 3.

Table 3. Kinetic and Isotherm Parameters for the As(III) Adsorption onto TiO<sub>2</sub> NFs<sup>a</sup>

adsorbents	amorphous	anatase	anatase/rutile	rutile
Pseudosecond-Order Model				
$q_{e,exp}/\text{mmol}\cdot\text{g}^{-1}$	0.0469	0.0373	0.0258	0.0162
$k_2\cdot 10^3/\text{g}\cdot\text{mmol}^{-1}\cdot\text{h}^{-1}$	$0.343 \pm 0.139$	$0.229 \pm 0.070$	$0.162 \pm 0.042$	$0.116 \pm 0.020$
$q_{e,cal}/\text{mmol}\cdot\text{g}^{-1}$	$0.0493 \pm 0.0015$	$0.0395 \pm 0.0011$	$0.0282 \pm 0.0008$	$0.0187 \pm 0.0006$
$\nu/\text{mmol}\cdot\text{g}^{-1}\cdot\text{h}^{-1}$	$0.834 \pm 0.341$	$0.357 \pm 0.095$	$0.128 \pm 0.034$	$0.041 \pm 0.008$
$R^2$	0.9986	0.9987	0.9973	0.9957
Nonlinear Langmuir Model				
$q_m/\text{mmol}\cdot\text{g}^{-1}$	$0.0544 \pm 0.0024$	$0.0397 \pm 0.0015$	$0.0267 \pm 0.0010$	$0.0172 \pm 0.0007$
$K_L\cdot 10^3/\text{L}\cdot\text{mmol}^{-1}$	$3.690 \pm 0.512$	$2.931 \pm 0.418$	$2.694 \pm 0.372$	$2.214 \pm 0.328$
$R^2$	0.9913	0.9950	0.9943	0.9981
Linear Langmuir Model				
$q_m/\text{mmol}\cdot\text{g}^{-1}$	$0.0542 \pm 0.0021$	$0.0396 \pm 0.0014$	$0.0266 \pm 0.0009$	$0.0172 \pm 0.0007$
$K_L\cdot 10^3/\text{L}\cdot\text{mmol}^{-1}$	$3.701 \pm 0.556$	$3.062 \pm 0.425$	$2.717 \pm 0.378$	$2.219 \pm 0.334$
$R^2$	0.9972	0.9995	0.9997	0.9998

<sup>a</sup>  $q_{e,exp}$ : experimental adsorption capacity;  $q_{e,cal}$ : calculated adsorption capacity;  $k_2$ : pseudosecond-order rate constant;  $\nu$ : initial adsorption rate;  $q_m$ : maximum adsorption capacity;  $K_L$ : Langmuir constant; the uncertainty of parameters are expanded uncertainty with a 0.95 level of confidence ( $k = 2$ ).

Figure 7 demonstrates that the experimental data could be well-described with the pseudosecond-order kinetic model. The

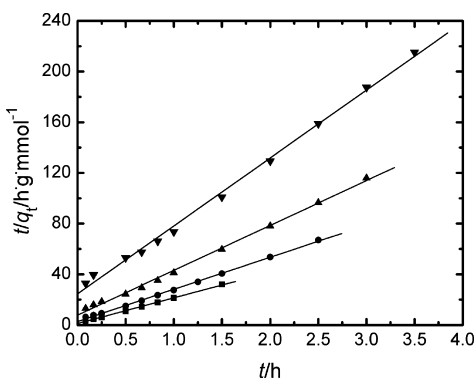


Figure 7. Pseudosecond-order kinetic plots of the As(III) adsorption data obtained on TiO<sub>2</sub> samples at  $298 \text{ K} \pm 1.6 \text{ K}$  and  $\text{pH } 7.0 \pm 0.1$ . ■, amorphous; ●, anatase; ▲, anatase/rutile; ▼, rutile TiO<sub>2</sub> NFs.

correlation coefficient ( $R^2$ ) values for the pseudosecond-order equation are 0.9940 to 0.9983, which are very close to 1. Moreover, the calculated ( $q_{cal}$ ) values are in agreement with the experimental ( $q_{exp}$ ) values, indicating that the pseudosecond-order kinetic model fitted the adsorption kinetic data accurately. The fit of the experimental data to this equation could indicate that chemical adsorption as the rate-limiting step of the adsorption mechanism and no involvement of mass transfer in solution,<sup>32</sup> which is similar to the research result of Penna et al.<sup>1</sup> The  $\nu$  of the amorphous TiO<sub>2</sub> NFs is higher than that of the crystalline TiO<sub>2</sub> NFs, which means amorphous TiO<sub>2</sub> NFs have a faster adsorption rate. The faster adsorption rate by amorphous TiO<sub>2</sub> NFs may be attributed to the relatively larger surface area, which provides a site to allow these adsorbate molecules to disperse freely and quickly.

**3.3. Adsorption Isotherms.** To investigate the effects of phase structures of TiO<sub>2</sub> NFs on As(III) adsorption capacity, various models can be used to analyze experimental data. The Langmuir isotherm is the most common model to analyze the equilibrium data of As(III) adsorption on TiO<sub>2</sub> materials reported in literature. Mathematically, the nonlinear model can be written as follows:<sup>33,34</sup>

$$q_e = \frac{q_m K_L C_e}{1 + K_L C_e} \quad (6)$$

The linear form is:

$$\frac{C_e}{q_e} = \frac{C_e}{q_m} + \frac{1}{q_m K_L} \quad (7)$$

where  $q_m$  is the As(III) maximum adsorption capacity on the materials ( $\text{mmol}\cdot\text{g}^{-1}$ ) and  $K_L$  is the Langmuir constant ( $\text{L}\cdot\text{mmol}^{-1}$ ) related to the binding energy of adsorption, and  $C_e$  is the equilibrium concentration ( $\text{mmol}\cdot\text{kg}^{-1}$ ).

The isotherm data have been analyzed with the Langmuir isotherm equations by both the nonlinear and the linear methods using the Origin 8.0 computer software spreadsheet, and the data fits are shown in Figures 8 and 9, respectively. The

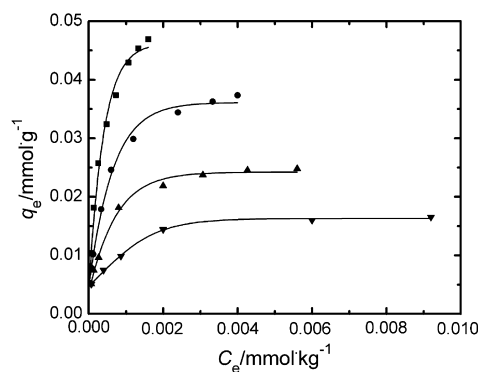
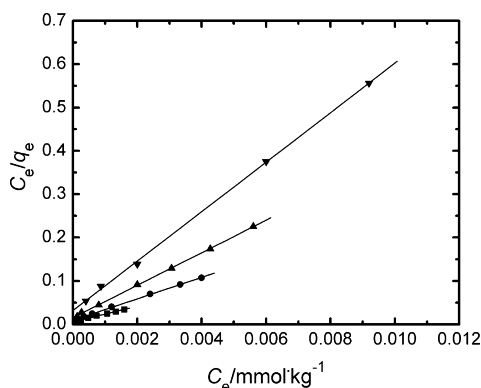


Figure 8. Nonlinear plots of the Langmuir isotherm model for As(III) adsorption onto TiO<sub>2</sub> NFs at  $298 \pm 1.6 \text{ K}$  and  $\text{pH } 7.0 \pm 0.1$ . ■, amorphous; ●, anatase; ▲, anatase/rutile; ▼, rutile TiO<sub>2</sub> NFs.

best fit constants calculated from the nonlinear and the linear analyses of the isotherm data are given in Table 3. The goodness of the model is quantified on the basis of the correlation coefficient ( $R^2$ ) values. The isotherm data are found to be well-fitted with both the nonlinear and the linear Langmuir isotherm, because values of the  $R^2$  are very high ( $R^2$  over 0.99). Thus, monolayer adsorption happened on the adsorbent surface. The obtained isotherm parameters from the Langmuir linear and the nonlinear equations are the same.



**Figure 9.** Linear plots of the Langmuir isotherm model for As(III) adsorption onto TiO<sub>2</sub> NFs at 298 ± 1.6 K and pH 7.0 ± 0.1. ■, amorphous; ●, anatase; ▲, anatase/rutile; ▼, rutile TiO<sub>2</sub> NFs.

There are no problems with transformations of the nonlinear Langmuir isotherm equation to linear forms.<sup>34</sup> As also displayed in Table 3, the  $q_m$  of the amorphous TiO<sub>2</sub> NFs for As(III) is higher than that of the crystalline TiO<sub>2</sub> NFs because of its higher pore volume and surface area.

A comparison of the  $q_m$ ,  $S_{BET}$ , and  $K_L$  of TiO<sub>2</sub> NFs with other metal oxides is presented in Table 4. It could be seen that the  $q_m$  of TiO<sub>2</sub> NFs is higher than those adsorbents except iron oxide nanoparticles. TiO<sub>2</sub> has proven to be effective for As(III) removal due to the presence of high affinity surface hydroxyl groups on the TiO<sub>2</sub> surface, which can form the surface complexes with As(III).<sup>12,35</sup> This is the reason TiO<sub>2</sub> has a smaller surface area but a higher adsorption capacity. Iron oxide nanoparticles have been the most often used adsorbent for As(III) removal in water with high surface area and adsorption capacities, but its disadvantages include relatively low robustness and mechanical strength.<sup>36</sup> Moreover, they are normally in the form of powders and have to be granulated or loaded into porous materials for fixed-bed adsorption in the actual application.<sup>37</sup> In contrast, TiO<sub>2</sub> NFs can be used directly and easily separated from aqueous solution after adsorption due to its the long nanofibrous morphology. The  $K_L$  is also an important parameter to evaluate the strength or affinity of the adsorbent for the As(III). The values of the  $K_L$  with both the amorphous TiO<sub>2</sub> NFs and the crystalline TiO<sub>2</sub> NFs are much higher than that of other metal oxides indicate that the As(III) is more strongly adsorbed onto TiO<sub>2</sub> NFs than other metal oxides due to their higher surface hydroxyl density. Thus, it can be concluded that TiO<sub>2</sub> NFs are very promising materials for As(III) removal from aqueous solution.

## 4. CONCLUSIONS

PVP/TiO<sub>2</sub> NFs have been synthesized by electrospinning, a simple and effective technology suitable for industrial production. Subsequently, the electrospun NFs were immersed in an aqueous CH<sub>3</sub>COOH (pH = 5) solution to produce the amorphous TiO<sub>2</sub> NFs or sintered in air for 3 h to produce the crystalline TiO<sub>2</sub> NFs. The obtained NFs were characterized by Fourier transform infrared spectrometer (FT-IR), X-ray photoelectron spectroscopy (XPS), X-ray diffraction (XRD), scanning electron microscopy (SEM), transmission electron microscopy (TEM), and N<sub>2</sub> adsorption–desorption isotherm measurements. Behaviors of As(III) adsorption on the TiO<sub>2</sub> samples have been investigated. The adsorption kinetics followed the pseudosecond-order kinetic model very well, and the equilibrium data are well-fitted with the Langmuir isotherm model. The surface area and pore volume play an important role in the adsorption of As(III) onto the TiO<sub>2</sub> NFs. The amorphous TiO<sub>2</sub> NFs have a higher adsorption capacity and rate than the crystalline TiO<sub>2</sub> NFs due to its higher surface area and pore volume. Because the amorphous TiO<sub>2</sub> NFs have a continuously long nanofibrous shape, high adsorption capacity, and fast adsorption rate, they can be promising materials for large-scale engineering applications for the removal of As(III) in water.

## AUTHOR INFORMATION

### Corresponding Author

\*E-mail: xiangli@jlu.edu.cn (X.L.), cwang@jlu.edu.cn (C.W.).  
Tel.: +86 431 85168292; fax: +86 431 85168292.

### Funding

This work was supported by the research grants from the National 973 Project (S2009061009), the National Natural Science Foundation of China (50973038).

### Notes

The authors declare no competing financial interest.

## REFERENCES

- (1) Pena, M. E.; Korfiatis, G. P.; Patel, M.; Lippincott, L.; Meng, X. G. Adsorption of As(V) and As(III) by nanocrystalline titanium dioxide. *Water Res.* **2005**, *39*, 2327–2337.
- (2) Mandal, S.; Padhi, T.; Patel, R. K. Studies on the removal of arsenic (III) from water by a novel hybrid material. *J. Hazard. Mater.* **2011**, *192*, 899–908.
- (3) Gupta, K.; Basu, T.; Ghosh, U. C. Sorption characteristics of arsenic (V) for removal from water using agglomerated nanostructure iron(III)-zirconium(IV) bimetal mixed oxide. *J. Chem. Eng. Data* **2009**, *54*, 2222–2228.
- (4) Singh, M.; Thanh, D. N.; Ulbrich, P.; Strnadova, N.; Stepanek, F. Synthesis, characterization and study of arsenate adsorption from

**Table 4.** Comparison of Adsorption Capacity of the TiO<sub>2</sub> NFs with Other Metal Oxides

adsorbent	pH	$S_{BET}$	$q_m \cdot 10^{-2}$	$K_L \cdot 10^3$	ref
		m <sup>2</sup> ·g <sup>-1</sup>	mmol·g <sup>-1</sup>	L·mmol <sup>-1</sup>	
natural goethite	7.5	2	0.49	0.32	38
activated alumina	7.6	370	0.24	0.64	39
mesoporous alumina	6.5 to 7.2	189	1.23	0.01	40
alumina/copper oxide	6.5 to 7.2	189	2.88	0.02	40
Fe <sub>3</sub> O <sub>4</sub> nanoparticles	7.0	179	61.41	0.01	41
γ-Fe <sub>2</sub> O <sub>3</sub> nanoparticles	6.0	168	99.77	0.43	42
amorphous TiO <sub>2</sub> NFs	7.0	65	5.42 to 5.44	3.14 to 4.25	this study
crystalline TiO <sub>2</sub> NFs	7.0	12 to 42	1.72 to 3.97	1.88 to 3.48	this study

aqueous solution by  $\alpha$ - and  $\beta$ -phase manganese dioxide nano-adsorbents. *J. Solid State Chem.* **2010**, *183*, 2979–2986.

(5) Dutta, P. K.; Ray, A. K.; Sharma, V. K.; Millero, F. J. Adsorption of arsenate and arsenite on titanium dioxide suspensions. *J. Colloid Interface Sci.* **2004**, *278*, 270–275.

(6) Bang, S. B.; Patel, M.; Lippincott, L.; Meng, X. G. Removal of arsenic from groundwater by granular titanium dioxide adsorbent. *Chemosphere* **2005**, *60*, 389–397.

(7) Liu, G.; Zhang, X.; Talley, J. W.; Neal, C. R.; Wang, H. Effect of NOM on arsenic adsorption by  $\text{TiO}_2$  in simulated As(III)-contaminated raw water. *Water Res.* **2008**, *42*, 2309–2319.

(8) Niu, H. Y.; Wang, J. M.; Shi, Y. L.; Cai, Y. Q.; Wei, F. S. Adsorption behavior of arsenic onto protonated titanate nanotubes prepared via hydrothermal method. *Microporous Mesoporous Mater.* **2009**, *122*, 28–35.

(9) Xu, Z. H.; Meng, X. G. Size effects of nanocrystalline  $\text{TiO}_2$  on As(V) and As(III) adsorption and As(III) photooxidation. *J. Hazard. Mater.* **2009**, *168*, 747–752.

(10) Jegadeesan, G.; Al-Abied, S. R.; Sundaram, V.; Choi, H.; Scheckel, K. G.; Dionysiou, D. Arsenic sorption on  $\text{TiO}_2$  nanoparticles: Size and crystallinity effects. *Water Res.* **2010**, *44*, 965–973.

(11) Piriä, M.; Martikainen, M.; Ainassaari, K.; Kuokkanen, T.; Keiski, R. L. Removal of aqueous As(III) and As(V) by hydrous titanium dioxide. *J. Colloid Interface Sci.* **2011**, *353*, 257–262.

(12) Guan, X. H.; Du, J. S.; Meng, X. G.; Sun, Y. K.; Sun, B.; Hu, Q. H. Application of titanium dioxide in arsenic removal from water: A review. *J. Hazard. Mater.* **2012**, *215–216*, 1–16.

(13) Rachel, A.; Subrahmanyam, M.; Boule, P. Comparison of photocatalytic efficiencies of  $\text{TiO}_2$  in suspended and immobilised form for the photocatalytic degradation of nitrobenzenesulfonic acids. *Appl. Catal. B: Environ.* **2002**, *37*, 301–308.

(14) Zhang, X. W.; Xu, S. Y.; Han, G. R. Fabrication and photocatalytic activity of  $\text{TiO}_2$  nanofiber membrane. *Mater. Lett.* **2009**, *63*, 1761–1763.

(15) Xu, S. Y.; Shi, Y.; Gook, S. Fabrication and mechanical property of nano piezoelectric fibers. *Nanotechnology* **2006**, *17*, 4497–4501.

(16) Vu, D.; Li, Z. Y.; Zhang, H. N.; Wang, W.; Wang, Z. J.; Xu, X. R.; Dong, B. Adsorption of Cu(II) from aqueous solution by anatase mesoporous  $\text{TiO}_2$  nanofibers prepared via electrospinning. *J. Colloid Interface Sci.* **2012**, *367*, 429–435.

(17) Li, D.; McCann, J.; Xia, Y. Electrospinning: a simple and versatile technique for producing ceramic nanofibers and nanotubes. *J. Am. Ceram. Soc.* **2006**, *89*, 1861–1869.

(18) Koo, C. M.; Ham, H. T.; Choi, M. H.; Kim, S. O. Characteristics of polyvinylpyrrolidone-layered silicate nanocomposites prepared by attrition ball milling. *Polymer* **2003**, *44*, 681–689.

(19) Shang, S. Q.; Jiao, X. L.; Chen, D. R. Template-free fabrication and photocatalytic properties of  $\text{TiO}_2$  hollow spheres. *ACS Appl. Mater. Interfaces* **2012**, *4*, 860–865.

(20) Li, Y. J.; Ma, M. Y.; Sun, S. G.; Yan, W. B.; Ouyan, Y. Z. Preparation of  $\text{TiO}_2$ -carbon surface composites with high photoactivity by supercritical pretreatment and sol-gel processing. *Appl. Surf. Sci.* **2008**, *254*, 4154–4158.

(21) Zhang, H.; Banfield, J. F. Understanding polymorphic phase transformation behavior during growth of nanocrystalline aggregates: insights from  $\text{TiO}_2$ . *J. Phys. Chem. B* **2000**, *104*, 3481–3487.

(22) Sun, Q.; Xu, Y. M. Evaluating intrinsic photocatalytic activities of anatase and rutile  $\text{TiO}_2$  for organic degradation in water. *J. Phys. Chem. C* **2010**, *114*, 18911–18918.

(23) Yu, J. G.; Yu, H. G.; Cheng, B.; Zhao, X. J.; Yu, J. C.; Ho, W. K. The effect of calcination temperature on the surface microstructure and photocatalytic activity of  $\text{TiO}_2$  thin films prepared by liquid phase deposition. *J. Phys. Chem. B* **2003**, *107*, 13871–13879.

(24) Li, D.; Xia, N. Electrospinning nanofibers reinventing the wheel. *Adv. Mater.* **2004**, *16*, 1151–1170.

(25) Dai, Y. Q.; Cobley, C. M.; Zeng, J.; Sun, Y. M.; Xia, Y. N. Synthesis of anatase  $\text{TiO}_2$  nanocrystals with exposed {001} facets. *Nano Lett.* **2009**, *9*, 2455–2459.

(26) Li, D.; Xia, Y. Fabrication of Titania Nanofibers by Electrospinning. *Nano Lett.* **2003**, *3*, 555–560.

(27) Yu, J. G.; Su, Y. S.; Cheng, B. Template-Free Fabrication and enhanced photocatalytic activity of hierarchical macro-/mesoporous titania. *Adv. Funct. Mater.* **2007**, *17*, 1984–1990.

(28) Sing, K. S. W.; Everett, D. H.; Haul, R. A. W.; Moscou, L. Reporting physisorption data for gas/solid systems with special reference to the determination of surface area and porosity. *Pure Appl. Chem.* **1985**, *57*, 603–619.

(29) Gregg, S. J.; Sing, K. S. W. *Adsorption, surface area and porosity*, 2nd ed.; Academic Press: London, 1982.

(30) Yu, J. G.; Su, Y. R.; Cheng, B.; Zhou, M. H.; Mole, J. Effects of pH on the microstructures and photocatalytic activity of mesoporous nanocrystalline titania powders prepared via hydrothermal method. *Catal. A: Chem.* **2006**, *258*, 104–112.

(31) Ho, Y. S.; McKay, G. Comparative of chemisorption kinetics models applied to pollutant removal on various sorbents. *J. Environ. Sci. Health, Part A* **1999**, *34*, 1179–1204.

(32) Zhang, Y.; Li, Q.; Sun, L.; Tang, R.; Zhai, J. High efficient removal of mercury from aqueous solution by polyaniline/humic acid nanocomposite. *J. Hazard. Mater.* **2010**, *175*, 404–409.

(33) Langmuir, I. The adsorption of gases on plane surfaces of glass, mica and platinum. *J. Am. Chem. Soc.* **1918**, *40*, 1361–1403.

(34) Kumar, K. V. Comparative analysis of linear and non-linear method of estimating the sorption isotherm parameters for malachite green onto activated carbon. *J. Hazard. Mater.* **2006**, *B136*, 172–202.

(35) Penna, M.; Meng, X. G.; Korfiatis, G. P.; Jing, C. Y. Adsorption mechanism of arsenic on nanocrystalline titanium dioxide. *Environ. Sci. Technol.* **2006**, *40*, 1257–1262.

(36) Zhang, K.; Dwivedi, V.; Chi, C.; Wu, J. Graphene oxide/ferric hydroxide composites for efficient arsenate removal from drinking water. *J. Hazard. Mater.* **2010**, *182*, 162–168.

(37) Deng, S.; Yu, G.; Xie, S.; Y, Q.; Huang, J.; Kuwaki, Y.; Iseki, M. Enhanced adsorption of arsenate on the aminated fibers: sorption behavior and uptake mechanism. *Langmuir* **2008**, *24*, 10961–10967.

(38) Gimenez, J.; Martinez, M.; Pablo, J.; Rovira, M.; Duro, L. Arsenic sorption onto natural hematite, magnetite, and goethite. *J. Hazard. Mater.* **2007**, *141*, 575–580.

(39) Singh, T. S.; Pant, K. K. Equilibrium, kinetics and thermodynamic studies for adsorption of As(III) on activated alumina. *Sep. Purif. Technol.* **2004**, *36*, 139–147.

(40) Pillewana, P.; Mukherjee, S.; Roychowdhury, T.; Das, S.; Bansiwala, A. Removal of As(III) and As(V) from water by copper oxide incorporated mesoporous alumina. *J. Hazard. Mater.* **2011**, *186*, 367–375.

(41) Feng, L.; Cao, M. H.; Ma, X. Y.; Zhua, Y. S.; Hua, C. W. Superparamagnetic high surface area  $\text{Fe}_3\text{O}_4$  nanoparticles as adsorbents for arsenic removal. *J. Hazard. Mater.* **2012**, *217–218*, 439–446.

(42) Lin, S.; Lu, D.; Liu, Z. Removal of arsenic contaminants with magnetic  $\gamma$ - $\text{Fe}_2\text{O}_3$  nanoparticles. *Chem. Eng. J.* **2012**, *211–212*, 46–52.